

Simulating Frequency-Domain Electron Paramagnetic Resonance: Bridging the Gap between Experiment and Magnetic Parameters for High-Spin Transition-Metal Ion Complexes

Joscha Nehr Korn,[†] Joshua Telser,[‡] Karsten Holldack,[§] Stefan Stoll,^{||} and Alexander Schnegg^{*,†}

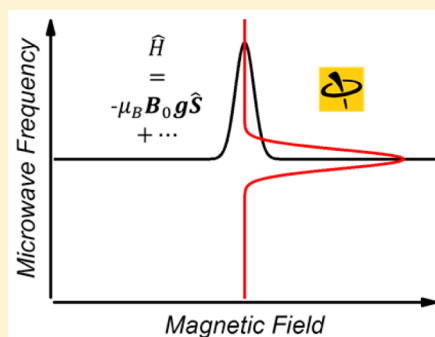
[†]Berlin Joint EPR Lab, Institute for Nanospectroscopy, Helmholtz-Zentrum Berlin für Materialien und Energie, Kekuléstraße 5, 12489 Berlin, Germany

[‡]Department of Biological, Chemical and Physical Sciences, Roosevelt University, 430 South Michigan Avenue, Chicago, Illinois 60605, United States

[§]Institute for Methods and Instrumentation for Synchrotron Radiation Research, Helmholtz-Zentrum Berlin für Materialien und Energie, Albert-Einstein-Straße 15, 12489 Berlin, Germany

^{||}Department of Chemistry, University of Washington, Box 351700, Seattle, Washington 98195, United States

ABSTRACT: We present a comparison of experimental and simulated frequency- and field-domain electron paramagnetic resonance (EPR) spectra of integer and half-integer high-spin transition-metal ion complexes. For the simulation of EPR spectra a new tool within the EPR simulation software *EasySpin* is introduced, which allows for field- and frequency-domain EPR simulations with the same theoretical model and the same set of spin Hamiltonian parameters. The utility of this approach is demonstrated on the integer-spin complexes $\text{NiBr}_2(\text{PPh}_3)_2$ and $[\text{Tp}_2\text{Mn}]\text{SbF}_6$ (both $S = 1$) and the half-integer-spin Fe(III) porphyrins, hemin (Fe(PPiX)Cl) and Fe(TPP)Cl (both $S = 5/2$). We demonstrate that the combination of field- and frequency-domain EPR techniques allows the determination of spin Hamiltonian parameters, in particular large zero-field splittings, with high accuracy.



1. INTRODUCTION

Paramagnetic complexes with multiple unpaired electrons ($S > 1/2$) frequently exhibit electron paramagnetic resonance (EPR) transitions over a wide range of energies, corresponding to frequencies from megahertz to terahertz. Major sources of these energy splittings are spin–orbit and spin–spin interactions among unpaired electrons that can lead to zero-field splitting (ZFS) of ground-state magnetic sublevels.¹ These interactions are sensitive to electronic structure and coordination environment.² In addition, they determine magnetic properties, e.g., in transition-metal ion or lanthanide-based single-molecule magnets.³ Hence, these interactions contain structurally highly relevant information. However, to accurately determine spin transition energies by EPR, the frequency of the applied radiation has to match the transition energy of interest. This is a significant technical challenge especially for systems with very large ZFS and unknown spin transition energies. One possibility to meet this challenge is high-field/high-frequency EPR (HF-EPR), which uses a single fixed frequency, typically in the 100–1000 GHz range, in combination with very broad field scans (e.g., 0–25 T).^{4,5} An alternative approach is frequency-domain EPR (FD-EPR), which employs broad frequency scans at a set of fixed magnetic fields. In this approach the possibility to match the desired frequency is obviously much higher. This is especially important for so-called “EPR silent” systems, which show no EPR transitions in conventional X-band (9–10 GHz/

0–1 T) and Q-band (33–35 GHz/0–2 T) spectrometers. An additional advantage of FD-EPR is that the ZFS can often be extracted directly from the zero-field spectrum. However, FD-EPR applications were until recently limited both by instrumental restrictions and the lack of versatile FD-EPR simulation programs. Technical issues of FD-EPR have been tackled recently by multiple approaches. Frequency sweeps can now be realized by employing a series of backward wave oscillators (BWOs) in frequency-domain magnetic resonance,⁶ laser-based time-domain terahertz spectroscopy,⁷ or Fourier transform infrared (FTIR)-based FD-FT THz EPR.^{8–12} The benefit of FD-EPR for the determination of ZFS was demonstrated for several mononuclear molecules,^{13–18} proteins,^{19,20} and polynuclear complexes.^{11,21–24} Furthermore, it was observed in these experiments that with FD-EPR the intensity of an EPR line can be mapped over a broad field-frequency range. This is often not possible in field sweep multifrequency EPR, where frequency-dependent variations of the microwave power and nonmagnetic microwave absorption in the sample may strongly influence the detected EPR response. The predictive power of FD-EPR can be increased by

Special Issue: Wolfgang Lubitz Festschrift

Received: April 30, 2015

Revised: June 22, 2015

complementary field-domain EPR measurements. For instance, g values and g anisotropies can be obtained with higher precision and resolution by field-domain EPR as compared to FD-EPR.²⁵ These parameters can then be used as fixed input parameters in the analysis of FD-EPR data for the determination of ZFS.¹⁹ Especially when the ZFS cannot be obtained from zero-field FD-EPR, this approach is extremely useful. Also, the opposite approach delivers valuable information. As will be shown in the following, HF-EPR is also very sensitive to small splittings originating from rhombic ZFS. However, measurements at a single EPR frequency are often not sufficient to determine a complete set of spin Hamiltonian parameters for transition-metal ions with large ZFS, which is cause for the employment of broad band FD-EPR approaches.

The proper analysis of a set of field- and frequency-domain EPR spectra requires a simulation approach which can calculate both domains under the same theoretical assumptions, in particular, one set of spin Hamiltonian parameters. For field-domain continuous-wave (CW) EPR spectra, least-squares fits of experimental data with simulations using a spin Hamiltonian formalism are standard nowadays. Various program packages for the simulation of field-domain EPR spectra, commercial as well as public domain, are available.^{26–33} The most complete and versatile numerical EPR package currently available is *EasySpin*.³⁴ It is widely used among EPR spectroscopists for planning and evaluating conventional EPR experiments. Its theory and experimental techniques are highly developed, which allows full analysis of spectra including line shapes and intensities. FD-EPR spectra have so far been mainly analyzed in terms of the positions of the EPR lines. The understanding of how absorption and dispersion modes, and both dielectric and magnetic dipoles, contribute to the detected signals in these experiments is in its infancy.³⁵ These issues are compounded by the lack of appropriate simulation tools.

Beyond this, FD-EPR simulations might be useful in the evaluation of new polarization agents for dynamic nuclear polarization (DNP).³⁶ In DNP, an EPR transition is driven in order to transfer the comparably large polarization difference of electron spin levels to that of nuclei and use this polarization enhancement for improved nuclear magnetic resonance (NMR) sensitivity.^{37–39} The spectral position at which the EPR is driven most effectively can be reached by varying the microwave (MW) frequency. However, for most potential polarization agents, only field-domain EPR spectra are available. It would be helpful to simulate FD-EPR spectra with magnetic parameters obtained from fitting the field-domain EPR spectrum.

This paper is organized as follows. In section II we introduce the employed theory, including the spin Hamiltonian, EPR transition probabilities, and how absorption and dispersion are obtained. In section III we describe the simulation program, including the new FD-EPR simulation functionality now implemented in *EasySpin*. Experimental details are provided in section IV. Finally, we demonstrate the validity and usefulness of the new simulation capabilities by comparison of experimental and simulated HF- and FD-EPR data in section V.

II. THEORY

The general spin Hamiltonian for a system with N_S electron spin centers and N_I magnetic nuclei used in *EasySpin* is

$$\hat{H} = \hat{H}_{B_0} + \hat{H}_{ZFS} + \hat{H}_{SS} + \hat{H}_{Nuc} \quad (1)$$

where the first term denotes the interaction of the spins with the external magnetic field, the second the ZFS, and the third the electron spin–spin interaction; the last term collects hyperfine and nuclear quadrupole interactions. \hat{H}_{B_0} is given by

$$\hat{H}_{B_0} = -\mathbf{B}_0 \cdot \hat{\boldsymbol{\mu}} \quad (2)$$

$$\hat{\boldsymbol{\mu}} = -\mu_B \sum_{i=1}^{N_S} \mathbf{g}_i \cdot \hat{\mathbf{S}}_i + \mu_N \sum_{j=1}^{N_I} \mathbf{g}_{N,j} \cdot \hat{\mathbf{I}}_j \quad (3)$$

where the external magnetic field is \mathbf{B}_0 ; $\hat{\boldsymbol{\mu}}$ is the vector operator for the total magnetic moment; μ_B and μ_N are the Bohr magneton and the nuclear magneton, respectively; \mathbf{g}_i and $\mathbf{g}_{N,j}$ denote the g matrices of the i th electron spin and the j th nuclei, which are not necessarily symmetric; $\hat{\mathbf{S}}_i = (\hat{S}_{ix}, \hat{S}_{iy}, \hat{S}_{iz})^T$ denotes the vector spin operator of the i th spin center with spin S_i , which can be different for each spin center; $\hat{\mathbf{I}}_j$ is the vector nuclear spin operator of the j th nucleus. Again, the nuclear spin I_j can be different for each nucleus. It is often convenient to specify the \mathbf{g}_i and $\mathbf{g}_{N,j}$ matrices (and the tensors in \hat{H}_{ZFS} , \hat{H}_{SS} , and \hat{H}_{Nuc}) in a local frame. This will be addressed in section III.

\hat{H}_{ZFS} is the zero-field splitting term. This term results from spin dipole–dipole interactions and spin–orbit coupling. It splits the otherwise degenerate energy levels of a single spin $S > 1/2$ even in the absence of an external magnetic field. It can be described in a perturbative way by^{2,40}

$$\hat{H}_{ZFS} = \sum_{i=1}^{N_S} \hat{\mathbf{S}}_i \cdot \mathbf{D}_i \cdot \hat{\mathbf{S}}_i \quad (4)$$

with \mathbf{D}_i being the 3×3 matrix of the ZFS tensor. Usually, it is symmetric; however, *EasySpin* is not restricted to such \mathbf{D}_i . For a single spin center it is convenient to define \mathbf{D}_i in a local frame in which \mathbf{D}_i is diagonal and the z -axis is the main anisotropy axis. Then the ZFS can be expressed as⁴¹

$$\hat{H}_{ZFS} = \sum_{i=1}^{N_S} \left[D_i \left(\hat{S}_{z,i}^2 - \frac{1}{3} S_i(S_i + 1) \right) + E_i (\hat{S}_{x,i}^2 - \hat{S}_{y,i}^2) \right] \quad (5)$$

\hat{H}_{ZFS} can also include higher-order terms using the Stevens operators.^{42–45} \hat{H}_{SS} and \hat{H}_{Nuc} are defined as usual in the EPR literature.⁴¹

Based on the general spin Hamiltonian in eq 1, the eigenenergies E_n and associated states $|n\rangle$ of the system at a fixed field can be calculated via matrix diagonalization. An EPR transition between states $|i\rangle$ and $|f\rangle$ can be observed if the energy of the MW radiation, $E_{MW} = h\nu$, with the MW frequency ν , is equal to the energy difference between the states, i.e., $E_{MW} = E_f - E_i$.

The EPR transition probability is according to time-dependent perturbation theory:⁴²

$$\rho_{i,f} \propto |\mathbf{B}_1 \cdot \langle f | \hat{\boldsymbol{\mu}} | i \rangle|^2 (p_i - p_f) \quad (6)$$

where \mathbf{B}_1 is the magnetic field component of the MW radiation and p_i and p_f are the populations of the initial and final states, respectively. In most cases, they are thermally populated and described by Boltzmann statistics. On the basis of eq 6, we have recently derived general, representation-independent expressions for the EPR transition probability for (almost) all types of

MW polarization and all possible experimental geometries (including Voigt and Faraday geometries).⁴⁶

Resonance frequencies at a fixed field are straightforwardly obtained, while the fast and robust determination of resonance fields for field sweeps is more involved.^{29–34,47,48} The EPR lines are broadened by the finite lifetime and/or by statistical effects, such as site-to-site variation of parameters within the sample. The former results in Lorentzian and the latter commonly in Gaussian line shapes. The overall absorption spectrum is the imaginary component of the complex dynamic magnetic susceptibility: $\chi = \chi' - i\chi''$. The dispersion spectrum can be obtained by the Kramers–Kronig relations.^{49,50} Using reasonable approximations,⁵¹ absorption and dispersion lineshapes and their derivatives can be calculated analytically for Lorentzians and Gaussians. If χ'' contains only a Lorentzian centered around ν_0 with full width at half-maximum σ , one obtains (derivatives are obtained as analytical expressions)

$$\chi'(\nu) = -\frac{2\sqrt{3}}{\pi\sigma^2} \frac{\nu - \nu_0}{1 + 4\left(\frac{\nu - \nu_0}{\sigma}\right)^2} \quad (7)$$

$$\chi''(\nu) = \frac{2}{\pi\sigma} \frac{1}{1 + 4\left(\frac{\nu - \nu_0}{\sigma}\right)^2} \quad (8)$$

Derivatives for Gaussians are obtained as follows. Assuming that χ'' contains a Gaussian centered around ν_0 with full width at half-maximum σ , then the n th derivative is given by^{51,52}

$$\chi'''(\nu) = \sqrt{\frac{2}{\pi}} \frac{1}{\Gamma^2 \sqrt{2 \ln 2}} \left(\frac{-2}{\Gamma}\right)^n H_n(k(\nu)) \exp\left[-\left(\frac{k(\nu)}{2}\right)^2\right] \quad (9)$$

$$\chi^{(n)}(\nu) = \frac{\sqrt{2}}{\pi\Gamma^2} \left(\frac{\sqrt{2}}{\Gamma}\right)^n [H_n(k(\nu)) F(k(\nu)) - G_{n-1}(k(\nu))] \quad (10)$$

with $k(\nu) = 2[(\nu - \nu_0)/\Gamma]$ and $\Gamma = \sigma/(2 \ln 2)^{1/2}$, the Hermite polynomials $H_n(x)$, and the Dawson function $F(x) = e^{-x^2} \int_0^x e^{t^2} dt$. $G_n(x)$ is recursively defined as $G_n(x) = 2xG_{n-1}(x) - 2nG_{n-2}(x)$ with $G_0(x) = 1$ and $G_{-1}(x) = 0$.⁵² With these equations, any harmonic of any admixture of absorption and dispersion spectra can be calculated.

III. SIMULATION PROGRAM

Here we describe the new functionality added to *EasySpin* for frequency-domain EPR spectra (as of version 5). We start with new functionalities which are general to the simulation program and therefore also apply to field-domain EPR simulations.

Simulation of the dispersion signal, and hence also mixtures of absorption and dispersion, was so far possible only for EPR lines with a Lorentzian component in the line shape. Equations 9 and 10 are now implemented and allow one to simulate all harmonics of Gaussian lines both in absorption and dispersion modes. For the Dawson function, an efficient numerical implementation is used.⁵³

Because of the lack of general expressions for the EPR transition probability, simulations were so far limited to experiments with linearly polarized MW radiation with B_1 either parallel or perpendicular to B_0 . Hence, spectra from beam experiments, used in HF- and FD-EPR, could not be simulated. Recently, we developed very general expressions for the EPR transition probability.⁴⁶ They are now included in

EasySpin and allow simulations for all types of MW polarization and for general experimental geometry. For increased consistency, the handling of transformations between coordination frames for the tensors, molecules, and crystal and for the laboratory is changed compared to previous versions of *EasySpin*. The transformation between the frames is reached via rotations parametrized by Euler angles.

$$\mathbf{R}(\alpha, \beta, \gamma) = \mathbf{R}_z(\gamma)\mathbf{R}_y(\beta)\mathbf{R}_z(\alpha) \quad (11)$$

$$\text{with } \mathbf{R}_z(\varphi) = \begin{pmatrix} \cos \varphi & \sin \varphi & 0 \\ -\sin \varphi & \cos \varphi & 0 \\ 0 & 0 & 1 \end{pmatrix}$$

$$\text{and } \mathbf{R}_y(\varphi) = \begin{pmatrix} \cos \varphi & 0 & -\sin \varphi \\ 0 & 1 & 0 \\ \sin \varphi & 0 & \cos \varphi \end{pmatrix}$$

For beam experiments, the laboratory frame is defined by the direction of the external magnetic field, B_0 , and the direction of propagation, k . We define z_L , the laboratory frame z -axis, along B_0 and y_L , the laboratory frame y -axis, in the plane defined by k and B_0 (see Figure 1a). The angle γ_k is between B_0 and k . In the laboratory frame, the direction of k is then

$$\frac{\mathbf{k}}{|\mathbf{k}|} = (0, \sin \gamma_k, \cos \gamma_k)^T \quad (12)$$

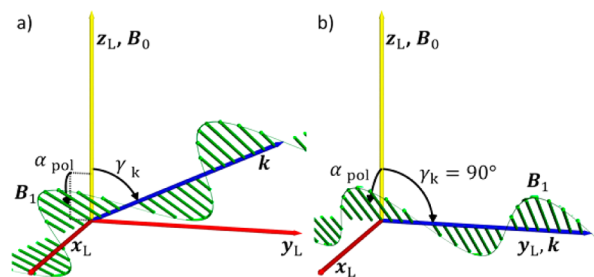


Figure 1. Sketch of B_1 in the laboratory frame. The oscillating B_1 (green arrows) is always in the plane normal to the propagation direction k . The red arrows depict the axes of the laboratory frame, L . The yellow arrow depicts B_0 . The angle γ_k between B_0 and k and the polarization angle α_{pol} are shown. In panel a, a general example is shown; in panel b, the Voigt geometry ($k \perp B_0$) is shown.

If linear polarized MW radiation is used, then the direction of B_1 is also needed. B_1 is perpendicular to k and uniquely defined by the polarization angle α_{pol} , the angle between B_1 and the (k, B_0) plane. Therefore, the direction of B_1 is in the laboratory frame

$$\frac{\mathbf{B}_1}{|\mathbf{B}_1|} = (\sin \alpha_{\text{pol}}, -\cos \gamma_k \cos \alpha_{\text{pol}}, \sin \gamma_k \cos \alpha_{\text{pol}})^T \quad (13)$$

In most EPR experiments, a resonator is used, for which k is not defined. However, to allow parallel and perpendicular B_1 resonator geometries, γ_k has to be set to 90° (see Figure 1b).

The Hamiltonian given in section II is defined in the molecular frame. This frame is molecule-fixed but otherwise essentially arbitrary. It is convenient to define its axes along symmetry axes of the studied molecule, if present. The tensors used in the Hamiltonian are not necessarily diagonal in this frame; however, for each of these tensors, a frame exists in

which it is diagonal. This is the corresponding tensor frame. The program provides the flexibility to enter the tensors either in the molecular frame or in their tensor frame together with the Euler angles for the rotation from the molecular frame to the tensor frame. If the molecular frame is not aligned with the axes of the crystal, the Euler angles for the transformation from the crystal frame to the molecular frame can be given. Finally, the crystal is oriented in the instrument, so that the Euler angles for the transformation from the crystal frame to the laboratory frame must be provided. Hence, a tensor T , diagonal in its tensor frame, is in the laboratory frame

$$T_L = R_{TL} T_{TL}^T \quad (14)$$

where

$$R_{TL} = R(\alpha_{CL}, \beta_{CL}, \gamma_{CL}) R^T(\alpha_{CM}, \beta_{CM}, \gamma_{CM}) R^T(\alpha_{MT}, \beta_{MT}, \gamma_{MT})$$

α_{MT} , β_{MT} , and γ_{MT} are the Euler angles for the transformation from the molecular frame to the tensor frame; α_{CM} , β_{CM} , and γ_{CM} are the Euler angles for the transformation from the crystal frame to the molecular frame; and α_{CL} , β_{CL} , and γ_{CL} are the Euler angles for the transformation from the crystal frame to the laboratory frame.

Even though FD-EPR experimentally differs substantially from field-domain EPR, most aspects of the numeric simulation are similar. Therefore, the simulation of frequency-domain EPR spectra is written as an extension of the *EasySpin* CW field-domain EPR simulation routine called *pepper*. Resonance frequencies and transition probabilities are obtained using eq 6 by diagonalization of eq 1 and with general expressions for the EPR transition probability.⁴⁶ Final spectra are obtained by introducing line broadening onto the calculated stick spectrum. This broadening can be Lorentzian, Gaussian, or Voigtian. It is also possible to include isotropic and anisotropic Gaussian distributions in the magnetic parameters, i.e., strains, which lead to a Gaussian broadening.³⁴ All strains can be used both for field- and frequency-sweeps without unit conversion. Additional convolutional line broadening is given in millitesla for field sweeps and megahertz for frequency sweeps.

A minimal example, which provides both field- and frequency-domain spectrum of a $S = 1$ system, is given in Scheme 1.

Scheme 1

```
clear
Sys.S = 1;
Sys.D = 1000; % MHz
Sys.DStrain = 50; % MHz

ExpField.mwFreq = 9.6; % GHz
ExpField.Range = [280 400]; % mT
pepper(Sys, ExpField); % field sweep

ExpFreq.Field = 343; % mT
ExpFreq.mwRange = [8 11]; % GHz
pepper(Sys, ExpFreq); % frequency sweep
```

For frequency-domain spectra, the zeroth harmonic is the default, while for field-swept spectra, the first harmonic is calculated by default.

The above-described new functionalities are included in *EasySpin* release 5, which is available free of charge from

easyspin.org, where detailed documentation and examples can be found.

IV. EXPERIMENTAL METHODS

A. Samples. Hemin (Fe(PPIX)Cl, chloro[3,7,12,17-tetramethyl-8,13-divinylporphyrin-2,18-dipropionato(2-)]iron(III)) and Fe(TPP)Cl (chloro(5,10,15,20-tetraphenylporphyrin)iron(III)) were both obtained from Aldrich and used as received. $\text{NiBr}_2(\text{PPh}_3)_2$ (PPh_3 = triphenylphosphine) was prepared as previously described.⁵⁴ The unit cell of crystals was checked, and the dimensions conformed to those of the reported structure.⁵⁵ $[\text{Tp}_2\text{Mn}]\text{SbF}_6$ (Tp = hydridotris(pyrazol-1-yl)borate) was previously prepared and characterized.¹³ The FD-FT THz-EPR samples were obtained by mixing approximately 50–100 mg of the sample either with polyethylene (PE) (for hemin) or PTFE (for the others) powder, finely ground and pressed to a pellet with 4650 bar applied pressure.

B. FD-FT THz-EPR. FD-EPR spectra were measured on the frequency-domain Fourier transform (FD-FT) THz-EPR spectrometer at the electron storage ring BESSY II, which is described in more detail elsewhere.^{11,19} This setup employs broadband terahertz radiation emitted by a Hg arc lamp or coherent synchrotron radiation for EPR excitation (Table 1).

Table 1. Overview of Experimental Conditions

sample	exptl resolution of the FTIR spectrometer	radiation source	absorbance, reference temperature	MDS, field step
hemin	0.5 cm^{-1}	Hg-arc lamp	36 K	0.5 T
Fe(TPP)Cl	0.2 cm^{-1}	synchrotron	20 K/36 K ⁵⁶	0.1 T
$\text{NiBr}_2(\text{PPh}_3)_2$	0.1 cm^{-1}	synchrotron		0.2 T

For EPR detection, a variety of He-cooled bolometers can be mounted at the end of the quasioptical transmission line. To discriminate between frequency-dependent variations in the excitation spectrum and the terahertz absorption properties of the sample from the EPR signals, reference spectra have to be recorded. In this work, two alternative methods were used for this purpose. In the first approach, EPR spectra are measured as FD-FT THz-EPR absorbance spectra (AS) where the absorbance is $A = \log_{10}(I_{\text{high}}/I_{\text{low}})$, where I_{high} and I_{low} are the intensities measured at elevated and low temperatures, respectively. By dividing spectra taken at different temperatures, changes in the spin level population are monitored as EPR-induced transmission changes. However, nonmagnetic absorption is oftentimes temperature-dependent and therefore difficult to distinguish from spin population changes. Purely magnetic absorption changes may be obtained by dividing two spectra taken at the same (preferably low) temperature but at two different external magnetic fields. The resulting magnetic field division FD-FT THz-EPR spectra (MDS) are sensitive to magnetic field-induced shifts of the magnetic absorption. Throughout this work, MDS are obtained by dividing high field by low field spectra and indexed by the lower field value. At very low temperatures, minima and maxima in the MDS then correspond to ground-state spin transitions at the lower and the higher field, respectively.

C. High-Field/High-Frequency EPR. HF-EPR measurements of Fe(TPP)Cl were measured on an EleXsys 780 EPR 263 GHz/12 T spectrometer. Fe-TPP was finely ground, filled into a PTFE sample holder, mounted in a nonresonant sample holder, and immersed into the sample cryostat. CW EPR

measurements were performed at a MW frequency of 262.4 GHz and a temperature of 5 K, with an incident MW power of 15 mW and 100 kHz field modulation with modulation amplitude of 40 G peak-to-peak.

V. RESULTS AND ANALYSIS

A. EPR Transition Energies of Integer and Half-Integer Transition-Metal Ions with Large ZFS. Figure 2 depicts

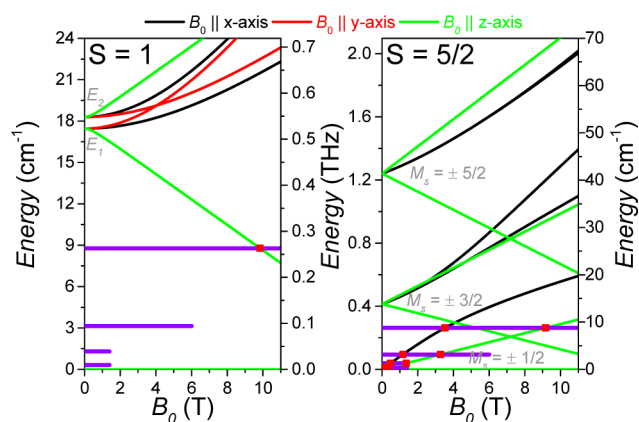


Figure 2. Calculated magnetic field dependency of energy levels for integer ($S = 1$ [Tp_2Mn]SbF₆, left) and half-integer ($S = 5/2$ hemin, right) systems. The energy levels are shown with respect to the corresponding ground state, i.e., the difference in energy to the ground state is plotted. The magnetic field is either applied parallel to the main anisotropy axis (the molecular z axis; green line) or perpendicular to it. Because of the significant rhombic anisotropy of [Tp_2Mn]SbF₆, the energy levels differ for B_0 alignment along the molecular x axis (black line) and y axis (red line). For hemin, on the contrary, no rhombic anisotropy was observed; therefore, all field directions perpendicular to the main anisotropy axis are equivalent (black line). The violet, horizontal lines indicate the measurement range of X-, Q-, and W-Band and 263 GHz EPR spectrometers. Red dots indicate calculated EPR transitions at these frequencies (no transitions are observed for [Tp_2Mn]SbF₆ below 263 GHz). The gray labels indicate the assignment of energy levels at zero magnetic field (see text for details). For better comparability with other techniques, transition energies are given in reciprocal centimeters and terahertz.

field-dependent spin energy levels for two important prototype integer ([Tp_2Mn]SbF₆ with Mn(III), $S = 1$, left panel) and half-integer (hemin with Fe(III), $S = 5/2$, right panel) high-spin transition-metal ions with large ZFS. For [Tp_2Mn]SbF₆, the three M_S sublevels are split by the axial ZFS (D) into a $M_S = 0$ singlet and the $M_S = \pm 1$ doublet separated by D . For positive D , usually referred to as easy-plane magnetic anisotropy, the singlet is the ground state, while for negative D , easy-axis type, the doublet is lowest in energy. The doublet is further split by rhombic ZFS (E), such that the two levels are separated by $E_1 = |D - E|$ and $E_2 = |D + E|$ from the singlet (M_S is a “good” quantum number only for $E = 0$). As a result of the magnetic anisotropy, the energy level splittings depend strongly on the direction of the applied magnetic field. For many integer spin systems and EPR spectrometers the splitting between singlet and doublet is too large to observe an EPR transition between these levels. EPR transitions within the doublet are strictly forbidden for $E = 0$ and are therefore hard to observe for systems with small E . Hence, these systems were recently classified as “EPR silent”, despite the fact that the spin system is paramagnetic.

The right panel of Figure 2 depicts the situation of a half-integer high-spin transition-metal ion with $S = 5/2$. Here, ZFS splits the six sublevels into three doublets. For the sake of simplicity, we will assume $E = 0$ in the following. However, it should be noted that also for $E \neq 0$ the doublets are not split in the absence of an external magnetic field because of the Kramers theorem.⁴² For $D > 0$, the $M_S = \pm 1/2$ doublet is lowest in energy. The $M_S = \pm 3/2$ doublet is separated from the ground state by $2D$. The $M_S = \pm 5/2$ doublet is another $4D$ higher in energy. In the case of $D < 0$ the order of the levels is inverted. These three zero-field doublets are each split by an applied magnetic field, and an EPR transition can be observed within the $M_S = \pm 1/2$ doublet, irrespective of the MW frequency. However, for direct determination of ZFS, a transition between the doublets has to be observed. Based on the energy level diagram depicted in Figure 2, EPR signals can be assigned to a particular transition; however, the exact extraction of spin Hamiltonian parameters requires the comparison of experimental and simulated EPR spectra, as will be demonstrated in the following for different integer and half-integer transition-metal ions.

B. FD-EPR of $S = 1$ ($\text{Ni}(\text{PPh}_3)_2\text{Br}_2$ and [Tp_2Mn]SbF₆). In the complex [Tp_2Mn]SbF₆, Mn(III) in an $S = 1$ low-spin configuration is stabilized by scorpionate (Tp) ligands.¹³ This complex exhibits a very large D of around 18 cm^{-1} . Recently, some of us determined the following ZFS and g values of [Tp_2Mn]SbF₆ from zero-field FD-FT THz-EPR and multi-frequency HF-EPR:¹³ $D = 17.874 \text{ cm}^{-1}$, $E = 0.42 \text{ cm}^{-1}$ ($E/D = 0.023$), $g_x = 2.065$, $g_y = 2.073$, $g_z = 1.978$. Figure 3 depicts

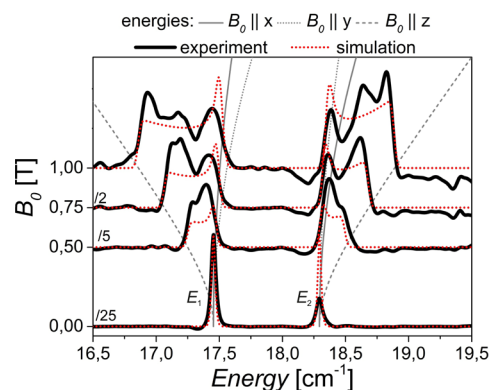


Figure 3. Experimental (solid black spectra) and simulated (red dotted spectra) field-dependent AS of [Tp_2Mn]SbF₆. AS taken at 0, 0.5, and 0.75 T are divided by 30, 5, and 2, respectively. Gray lines indicate EPR transition energies with respect to the ground state for B_0 alignment parallel to the molecular x - (solid), y - (dotted), and z -axis (dashed). The labels indicate the assignment of them at zero field. Simulation parameters are given in the text.

recently obtained AS¹³ alongside simulations. At zero field, two EPR transitions can be observed and are associated with ground-state transitions to excited states with energies E_1 and E_2 (see Figure 2). From these transitions, D and E can be directly determined. With increasing magnetic field, the two zero-field resonances further split. Using the recently obtained spin Hamiltonian parameters, the EPR lines and their field dependence can be simulated. However, relative intensities and details of the line shape slightly deviate from the experiment. This discrepancy may originate from partial orientational ordering of the [Tp_2Mn]SbF₆ powder sample in the presence

of an external magnetic field, which was not taken into account in the simulation.

The second $S = 1$ complex studied here is a member of the type $\text{Ni}(\text{PPh}_3)_2\text{X}_2$ ($\text{X}^- = \text{halide ion}$), which attracted early interest in coordination chemistry because of its geometry, which is roughly tetrahedral, as opposed to square planar as more commonly found for four-coordinate $\text{Ni}(\text{II})$.

Figure 4 depicts $\text{Ni}(\text{PPh}_3)_2\text{Br}_2$ EPR spectra recorded in MDS mode. Three features (labeled Ni1, Ni2, and Ni3) are visible, all

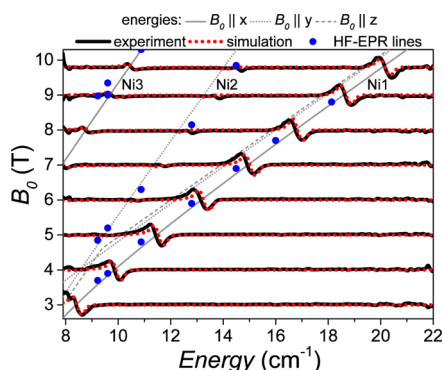


Figure 4. Experimental (black solid spectra) and simulated (red dotted spectra) MDS of $\text{Ni}(\text{PPh}_3)_2\text{Br}_2$. External magnetic fields at which the MDS were measured are indicated on the y-axis. Position of EPR lines observed recently with HF-EPR by Krzystek et al.⁵⁴ are indicated by blue dots. Gray lines indicate EPR transition energies with respect to the ground state for B_0 alignment parallel to the molecular x - (solid), y - (dotted), and z -axis (dashed). Simulation parameters are given in the text.

increasing in energy with increasing magnetic field. Ni1 shows no field-dependent dispersion; therefore, we assumed an isotropic g , $g_{\text{iso}} = 2.092$. It should be noted that the possibility of mapping relative EPR intensities over a very broad field and transition energy range, which is oftentimes not possible by other EPR techniques, provides additional insight. This isotropy reduces the expected field-dependency of the intensity drastically; therefore, we rescaled the simulation shown in Figure 4 for each magnetic field separately. Systematically varying the simulation parameters best match to the experimental spectra was obtained for $D = +4.7 \text{ cm}^{-1}$ and $|E| = 1.3 \text{ cm}^{-1}$ ($|E/D| = 0.28$). All features can be associated with transitions from the ground state to excited states E_1 (Ni3) and E_2 (Ni1, Ni2). Based on this model, the relative intensities and spectral positions of Ni1 and Ni3 can be excellently reproduced. However, Ni2 is simulated at slightly too low energy with the maximum deviation occurring at the highest field: 0.6 cm^{-1} at 9.8 T .

Krzystek et al. studied $\text{NiBr}_2(\text{PPh}_3)_2$ with multifrequency HF-EPR and magnetization measurements.⁵⁴ Their originally obtained data, which is in excellent agreement with our results (see Figure 4), was modeled with two different sets of spin Hamiltonian parameters: either $|D| = 4.5 \text{ cm}^{-1}$, $|E| = 1.5 \text{ cm}^{-1}$ ($|E/D| = 0.33$, the maximum rhombicity), $g_{xy} = 2.2$, $g_z = 2.0$; or $|D| = 4.2 \text{ cm}^{-1}$, $|E| = 1.0 \text{ cm}^{-1}$ ($|E/D| = 0.24$), $g_{\text{iso}} = 2.2$. Both are close to the parameter set determined by us. Especially the former parameter set can reproduce large parts of the MDS, although not as well as the parameter set determined by us. This comparison underlines that ZFS parameters can be obtained from FD-EPR with precision of at least a tenth of a wavenumber. Furthermore, this example highlights the

increased precision in ZFS parameters that is provided by simultaneous simulations of field- and frequency-domain EPR data with one spin Hamiltonian model.

C. FD- and HF-EPR of Fe(III) $S = 5/2$ Hemin and Fe(TPP)Cl. Hemin, a $S = 5/2$ high-spin Fe(III) protoporphyrin IX complex, is used for therapy in porphyria attacks.⁵⁷ The axial ZFS of its Fe(III) ion was determined to be $D \approx 6 \text{ cm}^{-1}$ ^{58–60} and refined in early FD-FT THz-EPR studies to $6.9\text{--}6.95 \text{ cm}^{-1}$.^{61,62} In the upper panel of Figure 5, zero-field AS of

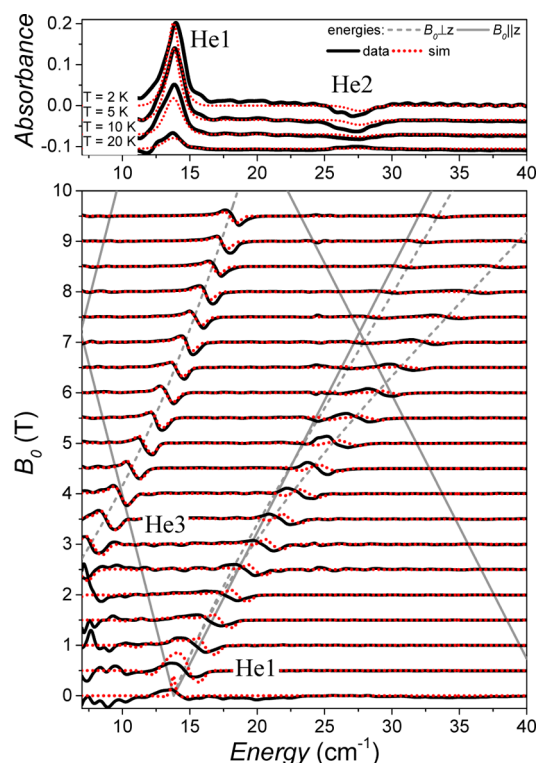


Figure 5. Experimental (black solid spectra) and simulated (red dotted spectra) AS (upper panel) and MDS (lower panel) of hemin. Data is shown with an offset for clarity. External magnetic fields at which the MDS were measured are indicated on the y-axis. Gray lines indicate EPR transition energies with respect to the ground state for B_0 alignment parallel (dashed) and perpendicular (solid) to z -axis. Simulation parameters are given in the text.

hemin are shown. These spectra are dominated by a pronounced resonance at 13.9 cm^{-1} , He1, which can be associated with a transition from the $M_S = \pm 1/2$ ground-state doublet to the $M_S = \pm 3/2$ doublet (see Figure 2). Around 27 cm^{-1} an additional broad minimum, He2, was identified. The negative absorbance ratio of He2 and the fact that it has approximately twice the energy of He1 allows for an assignment to a transition from the excited $M_S = \pm 3/2$ doublet to the excited $M_S = \pm 5/2$ doublet. In the MDS of hemin (lower panel of Figure 5), two pronounced field-dependent resonances were identified: He1 and an additional line, He3, which stems from a transition within the ground-state doublet (see Figure 2). Because we observed the ZFS splitting already in the absence of an external magnetic field, we could readily determine D to be $\sim 6.9 \text{ cm}^{-1}$. Further simulations of the MDS yielded $g_{\perp} = 1.95$ and $g_{\parallel} = 2.05$ and refined D to be 6.93 cm^{-1} . These simulations reproduce the hemin EPR spectra recorded in both FD-FT THz-EPR modalities very well. A comparison of MDS and AS in addition demonstrate that the observation of two resonances

over a broad field range provides higher precision in D than the zero-field spectrum, which is limited by the line width. Furthermore, simulations revealed that He3 , especially at higher fields, is sensitive to E ; therefore, we could infer $|E/D| < 0.02$.

Similar to hemin, $\text{Fe}(\text{TPP})\text{Cl}$ contains $\text{Fe}(\text{III})$ in high-spin $S = 5/2$ state, for which an axial ZFS of $D = 6\text{--}8\text{ cm}^{-1}$ was found.^{63,64} The ZFS values for $\text{Fe}(\text{TPP})\text{Cl}$ determined by multiple techniques are conveniently summarized in Table 1 of Hunter et al.⁶⁵ This very recent study employed inelastic neutron scattering (INS) and yielded $D = 6.33(8)\text{ cm}^{-1}$ ($E = 0$). This value is in good agreement with that ($D = 6.5\text{ cm}^{-1}$) of an early FD-FT THz-EPR study by Uenoyama⁶² and with our own results (see below). Figure 6 shows AS (upper panel) and

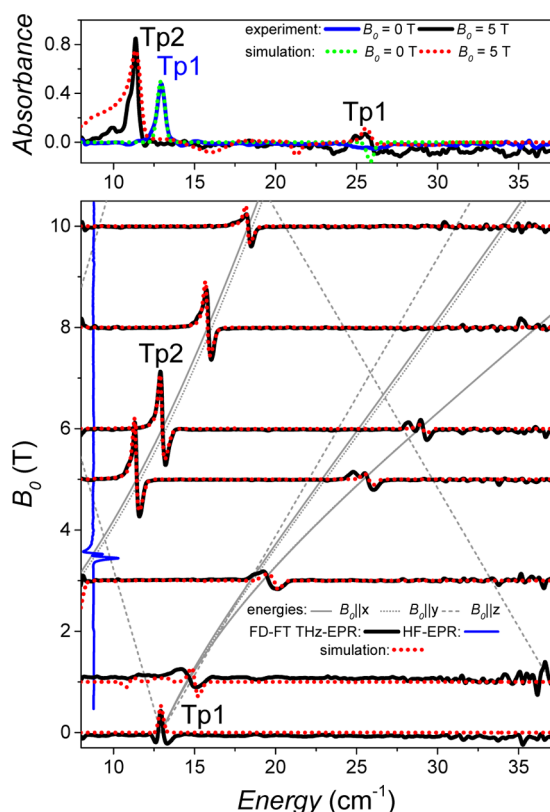


Figure 6. Experimental (black and blue solid spectra) and simulated (red and green dotted spectra) AS at 5 and 0 T (upper panel) and MDS (lower panel) of $\text{Fe}(\text{TPP})\text{Cl}$. On the y-axis external magnetic fields are given at which MDS were measured. Gray lines depict EPR transition energies with respect to the ground state for B_0 alignment parallel to the molecular x - (solid), y - (dotted), and z -axis (dashed). Simulation parameters are given in the text. The HF-EPR spectrum of $\text{Fe}(\text{TPP})\text{Cl}$ (blue solid spectrum) is plotted at the energy of the MW quantum.

MDS (lower panel) of $\text{Fe}(\text{TPP})\text{Cl}$. The spectra exhibit two main resonances, Tp1 and Tp2, which can be assigned to transitions from the ground-state doublet to the first excited doublet and within the ground-state doublet (see Figure 2), respectively. These are the same transitions which dominate the hemin spectra depicted in Figure 5; however, the resonance positions are shifted, indicating different ZFS.

The HF-EPR spectrum is shown in Figure 6 as a blue vertical line and is enlarged in Figure 7. The main peak of the spectrum is identical with resonance Tp2 in the MDS. However, whereas

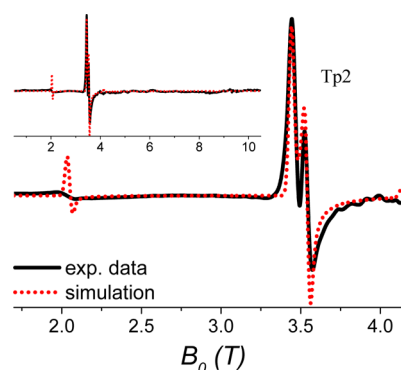


Figure 7. Experimental (black solid spectra) and simulated (red dotted spectra) HF-EPR spectra of $\text{Fe}(\text{TPP})\text{Cl}$ recorded at 262.4 GHz. The inset shows the full measured field range from 0.05 to 10.5 T. In the main panel, the field region in which spectral features were observed is magnified. Simulation parameters are given in the text.

Tp2 appears as a single unresolved peak in the MDS, a splitting was observed in the HF-EPR spectrum, which could be assigned to small rhombic ZFS. Simultaneous simulations of HF-EPR and FD-FT THz-EPR yielded the following spin Hamiltonian parameters: $D = 6.465\text{ cm}^{-1}$, $|E| = 0.02\text{ cm}^{-1}$ ($|E/D| = 0.003$), $g_{\perp} = 2.0$, and $g_{\parallel} = 1.95$. Thereby we were able to determine the axial and rhombic ZFS of $\text{Fe}(\text{TPP})\text{Cl}$ as well as differences in D for two structurally similar iron porphyrins with very high accuracy.

VI. CONCLUSION

We present an improved strategy for accurately determining large ZFS of integer and half-integer high-spin complexes. This strategy is based on combined field- and frequency-domain EPR data analyzed simultaneously with a new EPR simulation tool included in the EPR simulation software package *EasySpin*. This approach is demonstrated for two integer and two half-integer high-spin transition-metal ion complexes. However, it is generally applicable to any HS compound, including such important examples as $\text{Fe}(\text{II})$ in deoxy hemoglobin, $\text{Ni}(\text{II})$ in hydrogenases,^{66,67} and other function-determining cofactors in vital metal proteins. The method is limited neither to transition-metal ions nor to mononuclear complexes and can be utilized for lanthanide and multinuclear high-spin systems, e.g., single molecule magnets,³ where ZFS determines the magnetic properties.

AUTHOR INFORMATION

Corresponding Author

*E-mail: alexander.schnegg@helmholtz-berlin.de. Phone: +49 30 8062 41373. Fax: +49 30 8062 15074.

Notes

The authors declare no competing financial interest.

ACKNOWLEDGMENTS

This work has been supported and funded by Deutsche Forschungsgemeinschaft (DFG) priority program SPP 1601 and the University of Washington. The authors thank Prof. Robert Bittl (FU Berlin) for permitting measurements at the FD-FT THz-EPR setup and helpful discussions. Dirk Ponwitz (HZB) is acknowledged for technical support. It is a special pleasure and honor for us to contribute to the present Festschrift on the occasion of the 65th birthday of Prof. Wolfgang Lubitz. Wolfgang's outstanding contributions in

many important fields of science, in particular the development and application of novel EPR methods for the investigation of function-determining cofactors in proteins, has always been a great inspiration to us. Beyond this immense impact, Wolfgang's open-minded way of communicating and discussing science is a steady source of new views and thoughts, which continues to shape our scientific community in an extraordinary way.

REFERENCES

- (1) Boča, R. Zero-Field Splitting in Metal Complexes. *Coord. Chem. Rev.* **2004**, *248*, 757–815.
- (2) Neese, F. Zero-Field Splitting. In *Calculation of NMR and EPR Parameters. Theory and Applications*; Kaupp, M., Bühl, M., Malkin, V. G., Eds.; Wiley-VCH: Weinheim, 2004; pp 541–566.
- (3) Gatteschi, D.; Sessoli, R.; Villain, J. *Molecular Nanomagnets*; OUP: Oxford, 2006.
- (4) Krzystek, J.; Ozarowski, A.; Telser, J. Multi-Frequency, High-Field EPR as a Powerful Tool to Accurately Determine Zero-Field Splitting in High-Spin Transition Metal Coordination Complexes. *Coord. Chem. Rev.* **2006**, *250*, 2308–2324.
- (5) Telser, J.; Krzystek, J.; Ozarowski, A. High-Frequency and High-Field Electron Paramagnetic Resonance (HFEP): A New Spectroscopic Tool for Bioinorganic Chemistry. *JBIC, J. Biol. Inorg. Chem.* **2014**, *19*, 297–318.
- (6) van Slageren, J.; Vongtragool, S.; Gorshunov, B.; Mukhin, A. A.; Karl, N.; Krzystek, J.; Telser, J.; Müller, A.; Sangregorio, C.; Gatteschi, D.; Dressel, M. Frequency-Domain Magnetic Resonance Spectroscopy of Molecular Magnetic Materials. *Phys. Chem. Chem. Phys.* **2003**, *5*, 3837–3843.
- (7) Kozuki, K.; Nagashima, T.; Hangyo, M. Measurement of Electron Paramagnetic Resonance Using Terahertz Time-Domain Spectroscopy. *Opt. Express* **2011**, *19*, 24950–24956.
- (8) Mihály, L.; Talbayev, D.; Kiss, L. F.; Zhou, J.; Fehér, T.; Jánosy, A. Field-Frequency Mapping of the Electron Spin Resonance in the Paramagnetic and Antiferromagnetic States of LaMnO₃. *Phys. Rev. B: Condens. Matter Mater. Phys.* **2004**, *69*, 024414.
- (9) Talbayev, D.; Mihály, L.; Zhou, J. Antiferromagnetic Resonance in LaMnO₃ at Low Temperature. *Phys. Rev. Lett.* **2004**, *93*, 017202.
- (10) de Brion, S.; Darie, C.; Holzapfel, M.; Talbayev, D.; Mihály, L.; Simon, F.; Jánosy, A.; Chouteau, G. Spin Excitations in the Antiferromagnet NaNiO₂. *Phys. Rev. B: Condens. Matter Mater. Phys.* **2007**, *75*, 094402.
- (11) Schnegg, A.; Behrends, J.; Lips, K.; Bittl, R.; Holldack, K. Frequency Domain Fourier Transform THz-EPR on Single Molecule Magnets Using Coherent Synchrotron Radiation. *Phys. Chem. Chem. Phys.* **2009**, *11*, 6820–6825.
- (12) Ray, K.; Begum, A.; Weyhermüller, T.; Piligkos, S.; van Slageren, J.; Neese, F.; Wieghardt, K. The Electronic Structure of the Isoelectronic, Square-Planar Complexes [Fe^{II}(L)₂]²⁻ and [Co^{III}(L^{Bu})₂]⁻ (L²⁻ and (L^{Bu})²⁻ = Benzene-1,2-Dithiolates): An Experimental and Density Functional Theoretical Study. *J. Am. Chem. Soc.* **2005**, *127*, 4403–4415.
- (13) Forshaw, A. P.; Smith, J. M.; Ozarowski, A.; Krzystek, J.; Smirnov, D.; Zvyagin, S. A.; Harris, T. D.; Karunadasa, H. I.; Zadrozny, J. M.; Schnegg, A.; Telser, J. Low-Spin Hexacoordinate Mn(III): Synthesis and Spectroscopic Investigation of Homoleptic Tris-(Pyrazolyl)Borate and Tris(Carbene)Borate Complexes. *Inorg. Chem.* **2013**, *52*, 144–159.
- (14) Champion, P. M.; Sievers, A. J. Far IR Magnetic-Resonance in FeSiF₆·6H₂O and Fe(SPh)₄²⁻. *J. Chem. Phys.* **1977**, *66*, 1819–1825.
- (15) Brackett, G. C.; Richards, P. L.; Wickman, H. H. Far Infrared Spectra of Several Fe(III) Complexes with Spin S=3/2. *Chem. Phys. Lett.* **1970**, *6*, 75–78.
- (16) Brackett, G. C.; Richards, P. L.; Caughey, W. S. Far-Infrared Magnetic Resonance in Fe(III) and Mn(III) Porphyrins, Myoglobin, Hemoglobin, Ferrichrome-a, and Fe(III) Dithiocarbamates. *J. Chem. Phys.* **1971**, *54*, 4383–4401.
- (17) Telser, J.; van Slageren, J.; Vongtragool, S.; Dressel, M.; Reiff, W. M.; Zvyagin, S. A.; Ozarowski, A.; Krzystek, J. High-Frequency/High-Field EPR Spectroscopy of the High-Spin Ferrous Ion in Hexaqua Complexes. *Magn. Reson. Chem.* **2005**, *43*, S130–S139.
- (18) Vongtragool, S.; Gorshunov, B.; Dressel, M.; Krzystek, J.; Eichhorn, D. M.; Telser, J. Direct Observation of Fine Structure Transitions in a Paramagnetic Nickel(II) Complex Using Far-Infrared Magnetic Spectroscopy: A New Method for Studying High-Spin Transition Metal Complexes. *Inorg. Chem.* **2003**, *42*, 1788–1790.
- (19) Nehr Korn, J.; Martins, B. M.; Holldack, K.; Stoll, S.; Dobbek, H.; Bittl, R.; Schnegg, A. Zero-Field Splittings in Methb and Metmb with Aquo and Fluoro Ligands: A Fd-FT-THz EPR Study. *Mol. Phys.* **2013**, *111*, 2696–2707.
- (20) Champion, P. M.; Sievers, A. J. Far Infrared Magnetic Resonance of Deoxyhemoglobin and Deoxymyoglobin. *J. Chem. Phys.* **1980**, *72*, 1569–1582.
- (21) Dreiser, J.; Schnegg, A.; Holldack, K.; Pedersen, K. S.; Schau-Magnussen, M.; Nehr Korn, J.; Tregenna-Piggott, P.; Mutka, H.; Weihe, H.; Bendix, J.; Waldmann, O. Frequency-Domain Fourier-Transform Terahertz Spectroscopy of the Single-Molecule Magnet (NEt₄) [Mn₂(5-Brsalen)₂(MeOH)₂Cr(CN)₆]. *Chem. - Eur. J.* **2011**, *17*, 7492–7498.
- (22) Pedersen, K. S.; Dreiser, J.; Nehr Korn, J.; Gysler, M.; Schau-Magnussen, M.; Schnegg, A.; Holldack, K.; Bittl, R.; Piligkos, S.; Weihe, H.; Bendix, J.; Waldmann, O. A Linear Single-Molecule Magnet Based on [Ru^{III}(CN)₆]³⁻. *Chem. Commun.* **2011**, *47*, 6918–6920.
- (23) Dreiser, J.; Pedersen, K. S.; Schnegg, A.; Holldack, K.; Nehr Korn, J.; Sigrist, M.; Tregenna-Piggott, P.; Mutka, H.; Weihe, H.; Mironov, V. S.; Bendix, J.; Waldmann, O. Three-Axis Anisotropic Exchange Coupling in the Single-Molecule Magnets NEt₄[Mn^{III}(5-Brsalen)₂(MeOH)₂M^{III}(CN)₆] (M=Ru, Os). *Chem. - Eur. J.* **2013**, *19*, 3693–3701.
- (24) van Slageren, J.; Vongtragool, S.; Mukhin, A.; Gorshunov, B.; Dressel, M. Terahertz Faraday Effect in Single Molecule Magnets. *Phys. Rev. B: Condens. Matter Mater. Phys.* **2005**, *72*, 020401.
- (25) Schnegg, A.; Dubinskii, A. A.; Fuchs, M. R.; Grishin, Y. A.; Kirilina, E. P.; Lubitz, W.; Plato, M.; Savitsky, A.; Mobius, K. High-Field EPR, ENDOR and ELDOR on Bacterial Photosynthetic Reaction Centers. *Appl. Magn. Reson.* **2007**, *31*, 59–98.
- (26) Lund, A.; Andersson, P.; Eriksson, J.; Hallin, J.; Johansson, T.; Jonsson, R.; Löfgren, H.; Paulin, C.; Tell, A. Automatic Fitting Procedures for EPR Spectra of Disordered Systems: Matrix Diagonalization and Perturbation Methods Applied to Fluorocarbon Radicals. *Spectrochim. Acta, Part A* **2008**, *69*, 1294–1300.
- (27) Lund, A.; Gustafsson, H.; Maruani, J.; Shiotani, M. Automatic Fitting to 'Powder' EPR Spectra of Coupled Paramagnetic Species Employing Feynman's Theorem. *Spectrochim. Acta, Part A* **2006**, *63*, 830–835.
- (28) van Veen, G. Simulation and Analysis of EPR Spectra of Paramagnetic Ions in Powders. *J. Magn. Reson.* **1978**, *30*, 91–109.
- (29) Hanson, G. R.; Gates, K. E.; Noble, C. J.; Griffin, M.; Mitchell, A.; Benson, S. Xsophe-Sophe-Xeprview (R). A Computer Simulation Software Suite (V. 1.1.3) for the Analysis of Continuous Wave EPR Spectra. *J. Inorg. Biochem.* **2004**, *98*, 903–916.
- (30) Keijzers, C. P.; Reijerse, E. J.; Stam, P.; Dumont, M. F.; Gribnau, M. C. M. Magres - a General Program for Electron-Spin-Resonance, Endor and Esem. *J. Chem. Soc., Faraday Trans. 1* **1987**, *83*, 3493–3503.
- (31) Gaffney, B. J.; Silverstone, H. J. Simulation Methods for Looping Transitions. *J. Magn. Reson.* **1998**, *134*, 57–66.
- (32) Belford, G. G.; Belford, R. L.; Burkhalter, J. F. Eigenfields - Practical Direct Calculation of Resonance Fields and Intensities for Field-Swept Fixed-Frequency Spectrometers. *J. Magn. Reson.* **1973**, *11*, 251–265.
- (33) Gates, K. E.; Griffin, M.; Hanson, G. R.; Burrage, K. Computer Simulation of Magnetic Resonance Spectra Employing Homotopy. *J. Magn. Reson.* **1998**, *135*, 104–112.

- (34) Stoll, S.; Schweiger, A. Easyspin, a Comprehensive Software Package for Spectral Simulation and Analysis in EPR. *J. Magn. Reson.* **2006**, *178*, 42–55.
- (35) Kirchner, N.; van Slageren, J.; Dressel, M. Simulation of Frequency Domain Magnetic Resonance Spectra of Molecular Magnets. *Inorg. Chim. Acta* **2007**, *360*, 3813–3819.
- (36) Hu, K. N.; Song, C.; Yu, H. H.; Swager, T. M.; Griffin, R. G. High-Frequency Dynamic Nuclear Polarization Using Biradicals: A Multifrequency EPR Lineshape Analysis. *J. Chem. Phys.* **2008**, *128*, 052302.
- (37) Ardenkjaer-Larsen, J. H.; Fridlund, B.; Gram, A.; Hansson, G.; Hansson, L.; Lerche, M. H.; Servin, R.; Thaning, M.; Golman, K. Increase in Signal-to-Noise Ratio of > 10,000 Times in Liquid-State NMR. *Proc. Natl. Acad. Sci. U. S. A.* **2003**, *100*, 10158–10163.
- (38) Maly, T.; Debelouchina, G. T.; Bajaj, V. S.; Hu, K. N.; Joo, C. G.; Mak-Jurkauskas, M. L.; Sirigiri, J. R.; van der Wel, P. C. A.; Herzfeld, J.; Temkin, R. J.; Griffin, R. G. Dynamic Nuclear Polarization at High Magnetic Fields. *J. Chem. Phys.* **2008**, *128*, 052211.
- (39) Slichter, C. P. The Discovery and Renaissance of Dynamic Nuclear Polarization. *Rep. Prog. Phys.* **2014**, *77*, 072501.
- (40) Pilbrow, J. R. *Transition Ion Electron Paramagnetic Resonance*; Clarendon Press: Oxford, 1990.
- (41) Weil, J. A.; Bolton, J. R. *Electron Paramagnetic Resonance: Elementary Theory and Practical Applications*; Wiley: New York, 2007.
- (42) Abragam, A.; Bleaney, B. *Electron Paramagnetic Resonance of Transition Ions*; Dover Publications, Inc.: New York, 1986.
- (43) Rudowicz, C.; Chung, C. Y. The Generalization of the Extended Stevens Operators to Higher Ranks and Spins, and a Systematic Review of the Tables of the Tensor Operators and Their Matrix Elements. *J. Phys.: Condens. Matter* **2004**, *16*, 5825–5847.
- (44) Ryabov, I. D. On the Generation of Operator Equivalents and the Calculation of Their Matrix Elements. *J. Magn. Reson.* **1999**, *140*, 141–145.
- (45) Al'tshuler, S. A.; Kozyrev, B. M. *Electron Paramagnetic Resonance in Compounds of Transition Elements*; Wiley: New York, 1974.
- (46) Nehrkorn, J.; Schnegg, A.; Holldack, K.; Stoll, S. General Magnetic Transition Dipole Moments for Electron Paramagnetic Resonance. *Phys. Rev. Lett.* **2015**, *114*, 010801.
- (47) Misra, S. K. Evaluation of Spin-Hamiltonian Parameters from EPR Data by Method of Least-Squares Fitting. *J. Magn. Reson.* **1976**, *23*, 403–410.
- (48) Glerup, J.; Weihe, H. Magnetic-Susceptibility and EPR-Spectra of μ -Cyano-Bis[Pentaamminechromium(III)] Perchlorate. *Acta Chem. Scand.* **1991**, *45*, 444–448.
- (49) Gorter, C. J.; Kronig, R. d. L. On the Theory of Absorption and Dispersion in Paramagnetic and Dielectric Media. *Physica* **1936**, *3*, 1009–1020.
- (50) Kronig, R. D. L. On the Theory of Dispersion of X-Rays. *J. Opt. Soc. Am.* **1926**, *12*, 547–556.
- (51) Pake, G. E.; Purcell, E. M. Line Shapes in Nuclear Paramagnetism. *Phys. Rev.* **1948**, *74*, 1184–1188.
- (52) Barakat, R. Derivatives of Dawsons Function. *J. Quant. Spectrosc. Radiat. Transfer* **1971**, *11*, 1729–1730.
- (53) Weideman, J. A. C. Computation of the Complex Error Function. *Siam J. Numer. Anal.* **1994**, *31*, 1497–1518.
- (54) Krzystek, J.; Park, J. H.; Meisel, M. W.; Hitchman, M. A.; Strateimer, H.; Brunel, L. C.; Telser, J. EPR Spectra from "EPR-Silent" Species: High-Frequency and High-Field EPR Spectroscopy of Pseudotetrahedral Complexes of Nickel(II). *Inorg. Chem.* **2002**, *41*, 4478–4487.
- (55) Jarvis, J. A. J.; Mais, R. H. B.; Owston, P. G. Stereochemistry of Complexes of Nickel(2) 0.2. Crystal and Molecular Structure of Dibromobis(Triphenylphosphine)Nickel(2). *J. Chem. Soc. A* **1968**, 1473–1486.
- (56) The reference for the absorbance in the absence of an external magnetic field was measured at a temperature of 20 K, and the low temperature was 5 K. The reference for the absorbance measured with an external magnetic field of 5 T was measured at 36 K, with the low-temperature spectrum measured at a temperature of 2 K.
- (57) Bickers, D. R. Treatment of the Porphyrins - Mechanisms of Action. *J. Invest. Dermatol.* **1981**, *77*, 107–113.
- (58) Johnson, C. E. Hyperfine Field of ^{57}Fe in Hemin. *Phys. Lett.* **1966**, *21*, 491–492.
- (59) Lang, G.; Marshall, W. Mossbauer Effect in Some Haemoglobin Compounds. *J. Mol. Biol.* **1966**, *18*, 385–404.
- (60) Marathe, V. R.; Mitra, S. Zero-Field Splitting in Hemin. *Chem. Phys. Lett.* **1973**, *19*, 140–142.
- (61) Richards, P. L.; Caughey, W. S.; Eberspaecher, H.; Feher, G.; Malley, M. Determination of Zero-Field Splitting of Fe^{3+} in Several Hemin Compounds. *J. Chem. Phys.* **1967**, *47*, 1187–1188.
- (62) Uenoyama, H. Far-Infrared Studies on Hemin and Hemin-Like Complexes. *Biochim. Biophys. Acta, Gen. Subj.* **1971**, *230*, 479–481.
- (63) Zhou, Y.; Bowler, B. E.; Eaton, G. R.; Eaton, S. S. Electron Spin-Lattice Relaxation Rates for High-Spin Fe(III) Complexes in Glassy Solvents at Temperatures between 6 and 298 K. *J. Magn. Reson.* **2000**, *144*, 115–122.
- (64) Marathe, V. R.; Mitra, S. Low-Temperature Magnetization Study on High-Spin Iron(III) Porphyrins. *J. Chem. Phys.* **1983**, *78*, 915–920.
- (65) Hunter, S. C.; Podlesnyak, A. A.; Xue, Z. L. Magnetic Excitations in Metalloporphyrins by Inelastic Neutron Scattering: Determination of Zero-Field Splittings in Iron, Manganese, and Chromium Complexes. *Inorg. Chem.* **2014**, *53*, 1955–1961.
- (66) Hans, M.; Buckel, W.; Bill, E. The Iron-Sulfur Clusters in 2-Hydroxyglutaryl-CoA Dehydratase from *Acidaminococcus Fermentans*. *Eur. J. Biochem.* **2000**, *267*, 7082–7093.
- (67) Duderstadt, R. E.; Brereton, P. S.; Adams, M. W. W.; Johnson, M. K. A Pure $\text{S=3/2 } [\text{Fe}_4\text{S}_4]^+$ Cluster in the A33Y Variant of *Pyrococcus Furiosus* Ferredoxin. *FEBS Lett.* **1999**, *454*, 21–26.

NOTE ADDED AFTER ASAP PUBLICATION

This paper published ASAP on July 24, 2015. Due to a production error, a correction was made to eq 3 and the revised version was reposted on July 27, 2015.